Numerical Studies of Droplet Interactions

Wadhwa A. R., Magi V.[*], Abraham, J.[+]

Maurice J. Zucrow Laboratories, School of Mechanical Engineering, Purdue University, West Lafayette, IN 47907-2014, USA
* Permanent affiliation - Department of Environmental Engineering and Physics, University of Basilicata, Potenza, Italy
+ Corresponding author – John Abraham: jabraham@ecn.purdue.edu

In this work, a numerical algorithm is developed for studying internal and external flows of deforming drops. The liquid phase is modeled as an incompressible fluid, while the gas phase is modeled as a compressible fluid. The interface separating the two phases is tracked in time by employing an unstructured grid for the two phases, which conforms to the deforming interface at all instants in time. Finite volume discretization of the conservative form of the governing equations is solved for both the phases. An implicit iterative procedure is adopted to simultaneously solve the governing equations of the two phases, along with the boundary conditions at the interface. The numerical accuracy of the code is assessed by comparing the computed drag coefficient for unsteady viscous flows past solid spheres for a range of Reynolds numbers with experimental values, comparing the computed transient drag of a decelerating solid sphere with prior computed results published in the literature, and comparing the computed behavior of an oscillating drop with the classical solution of the problem. As an additional contribution of this work, initial results of transient drag coefficients for decelerating and deforming drops are presented and compared with results for the solid sphere.

1. Introduction

In liquid injection, the intact liquid breaks up into drops within several diameters downstream of the orifice. These drops then undergo a variety of interactions among themselves and with the ambient gas. The interactions between the drops result in several outcomes as discussed in the literature [1,2]. Numerical studies of these drop-drop interactions have been reported [3,4,5,6], but much remains to be done. The interactions with the ambient gas result in momentum transfer between the drop and the gas, and in drop deformation and secondary break up. These interactions are also not well understood. In fact, in multidimensional spray models [7,8], the momentum transfer between the drop and the gas is estimated by employing drag correlations, which have been developed for solid spheres in steady flows. Recent work by Kim et al. [9] has shown that these drag coefficients are inadequate in *transient* flows even for solid spheres. Furthermore, it has been reported in the literature that steady drag coefficients for deforming spheres are different from those for solid spheres [10,11,12]. There have not been many studies of transient drag coefficients for drops though quasi-steady drag has been reported [13]. In fact, we are not aware of any numerical studies in the transient. The experimental work of Temkin and Mehta [14] indicates that the unsteady drag for decelerating flows is always larger than the steady drag for a solid sphere at the same Reynolds number, whereas in accelerating flows, the unsteady drag is observed to be smaller

than the corresponding steady drag of a solid at the same Reynolds number. The focus of our work is to numerically study the transient drag for drops, i.e., in decelerating and accelerating flows. In this paper, we will report some initial results.

In the next few sections, the governing equations for the two fluids, the physical model for the interface, the space and time discretizations employed in the numerical method along with the grid movement strategies are discussed. The computed drag coefficients for steady flow past a stationary sphere are then presented for a range of Reynolds numbers. This is followed by a comparison of the transient drag for a decelerating solid sphere with the prior work of Kim et al. [9], and a comparison of the analytical solution and computed results for an oscillating liquid drop. Following this, initial results of the transient drag coefficients of decelerating drops will be presented and related to drop deformation. The paper closes with summary and conclusions.

2. Numerical model

2.1. Governing equations

The computational model consists of a liquid drop surrounded by gas. The liquid drop is modeled as an incompressible fluid, while the gas phase is modeled as a compressible fluid. The two immiscible fluids are separated by an interface, which has constant surface tension.

To overcome the stiffness problem [15] associated with solving the time-dependent hyperbolic conservation equations for compressible flows at low Mach numbers, the equations are preconditioned to include a pseudo-time term, which has the same form as the physical time term. The converged solution in pseudo-time represents the transient solution of the governing equations in physical time. The solution of this preconditioned form of the equations is accurate for compressible flows with Mach numbers ranging from the incompressible limit to the supersonic regime [15]. The unsteady integral form of the governing equations for the compressible gas phase are:

$$\frac{\partial}{\partial t^*}\iiint_{V(t)} \mathbf{W}_g \, \mathrm{d}V + \frac{\partial}{\partial t}\iiint_{V(t)} \mathbf{W}_g \, \mathrm{d}V + \iint_{S(t)} \left(\mathbf{F}_c - \mathbf{F}_v\right)_g \bullet \hat{n} \, \mathrm{d}S = 0 \tag{1}$$

where

$$\mathbf{W}_g = \begin{pmatrix} \rho_g \\ \rho_g \vec{V}_g \\ \rho_g e_g \end{pmatrix}; \qquad \mathbf{F}_c = \mathbf{W}_g \left(\vec{V}_g - \vec{V}_s\right) + p_g \begin{pmatrix} 0 \\ \vec{\vec{\mathrm{I}}} \\ \vec{V}_g \end{pmatrix} \qquad \text{and} \qquad \mathbf{F}_v = \begin{pmatrix} 0 \\ \vec{\vec{\tau}}_g \\ -\vec{q}_g + \left(\vec{\vec{\tau}}_g \bullet \vec{V}_g\right) \end{pmatrix} \tag{2}$$

t is the physical time and t^* represents a pseudo-time. $S(t)$ is the surface area bounding the control volume $\nu(t)$ at time t. $\hat{n}$ is the unit normal vector pointing outward from the control volume $\nu(t)$. $\vec{V}_s$ is the velocity vector of the moving surface $S(t)$. ρ_g is the density, $\vec{V}_g$ is the velocity, e_g is the total specific energy, p_g is the pressure, $\vec{\vec{\tau}}_g$ is the viscous stress tensor, $\vec{q}_g$ is the heat flux vector of the gas phase in the control volume. $\vec{\vec{\mathrm{I}}}$ is the identity tensor. The set of conservation equations (Eq.(1)) is closed by employing the ideal gas equation of state.

An artificial compressibility method [16] is employed for the incompressible liquid phase. In this method, the governing equations are modified to include an unsteady term in pseudo-time. A solution of the modified equations that is steady in pseudo-time is identical to the instantaneous unsteady solution of the governing equations in physical time. The unsteady integral form of the governing equations for the incompressible liquid phase are:

Mass:
$$\frac{\partial}{\partial t^*}\iiint_{V(t)} p_l \, \mathrm{d}V + \rho_l \iint_{S(t)} \beta\left(\vec{V}_l \bullet \hat{n}\right) \mathrm{d}S = 0 \tag{3}$$

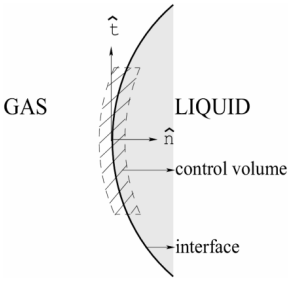

Fig. 1 Control volume employed to derive the interface conditions.

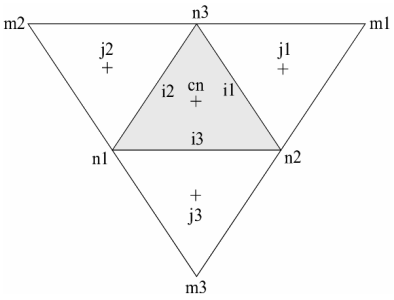

Fig. 2 A triangular control volume employed to illustrate the numerical discretization.

$$\textit{Momentum and Energy:}\quad \rho_l\left[\frac{\partial}{\partial t^*}\iiint_{V(t)}\mathbf{W}_l\,\mathrm{d}V+\frac{\partial}{\partial t}\iiint_{V(t)}\mathbf{W}_l\,\mathrm{d}V\right]+\iint_{S(t)}\left(\mathbf{F}_c-\mathbf{F}_v\right)_l\bullet\hat{n}\,\mathrm{d}S=0 \tag{4}$$

where

$$\mathbf{W}_l=\begin{pmatrix}\vec{V}_l\\ e_l\end{pmatrix};\qquad \mathbf{F}_c=\rho_l\mathbf{W}_l\left(\vec{V}_l-\vec{V}_s\right)+p_l\begin{pmatrix}\vec{\vec{\mathrm{I}}}\\ \vec{V}_l\end{pmatrix}\qquad\text{and}\qquad \mathbf{F}_v=\begin{pmatrix}\vec{\vec{\tau}}_l\\ -\vec{q}_l+\left(\vec{\vec{\tau}}_l\bullet\vec{V}_l\right)\end{pmatrix} \tag{5}$$

ρ_l is the density of the liquid phase and is assumed to be constant due to the incompressible fluid assumption. $\vec{V}_l$ is the velocity, e_l is the total specific energy, p_l is the pressure, $\vec{\vec{\tau}}_l$ is the viscous stress tensor, $\vec{q}_l$ is the heat flux vector of the liquid phase in the control volume. In the artificial compressibility method, the artificial density, ρ_l^*, is related to the pressure, p_l, by the artificial equation of state: $p_l = \beta\,\rho_l^*$, where β is the artificial compressibility factor and representative of an artificial speed of sound. The optimum value of β depends on the problem being solved.

2.2. *Physical modeling of interface*

Figure 1 shows the control volume employed in the derivation of the interface conditions. The assumptions made for the control volume analysis are: (1). Thickness of control volume is negligible at the interface, (2). Mass within the interface is negligible, and (3). Velocity at the interface is subjected to the no-slip condition. These assumptions result in the following transport equations:

$$\textit{Mass:}\qquad \rho_l\left[\left(\vec{V}_l-\vec{V}_{int}\right)\bullet\hat{n}\right]=\rho_g\left[\left(\vec{V}_g-\vec{V}_{int}\right)\bullet\hat{n}\right] \tag{6}$$

where $\vec{V}_{int}$ is the interface velocity vector. Since the two fluids on either side of the interface are assumed to be immiscible,

$$\vec{V}_l=\vec{V}_g=\vec{V}_{int} \tag{7}$$

$$\textit{Momentum normal to the interface:}\qquad p_l-\left(\hat{n}\bullet\vec{\vec{\tau}}_l\right)\bullet\hat{n}=p_g-\left(\hat{n}\bullet\vec{\vec{\tau}}_g\right)\bullet\hat{n}+\sigma\kappa \tag{8}$$

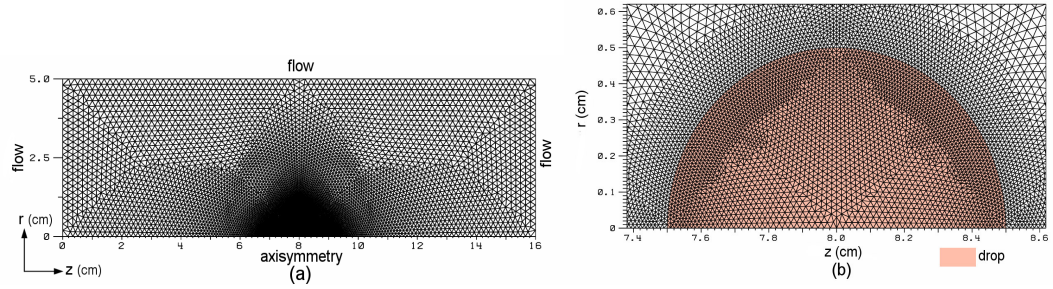

Fig. 3 Unstructured grid employed in liquid drop computations: (a) whole domain, (b) magnified view of the grid inside the liquid drop and in its vicinity.

Momentum tangential to the interface: $$\left(\hat{n}\bullet\vec{\vec{\tau}}_l\right)\bullet\hat{t}=\left(\hat{n}\bullet\vec{\vec{\tau}}_g\right)\bullet\hat{t} \tag{9}$$

Energy: $$p_l\left(\vec{V}_l\bullet\hat{n}\right)-\hat{n}\bullet\left(\vec{\vec{\tau}}_l\bullet\vec{V}_l\right)+\vec{q}_l\bullet\hat{n}=p_g\left(\vec{V}_g\bullet\hat{n}\right)-\hat{n}\bullet\left(\vec{\vec{\tau}}_g\bullet\vec{V}_g\right)+\vec{q}_g\bullet\hat{n}+\sigma\kappa\left(\vec{V}_{int}\bullet\hat{n}\right) \tag{10}$$

where σ is the surface tension and κ is the curvature of the interface.

2.3. Space discretization

The governing equations are solved in the cylindrical coordinate system (r,θ,z). The flow is assumed to be axisymmetric in this work and so, a two-dimensional grid is employed to discretize the computational domain. The formulation is valid for full three-dimensional simulations. An unstructured grid with triangular elements has been employed in this work. The grid is generated separately for each phase with the interface as a common boundary. This allows the unstructured grid to conform to the irregular shape of the interface at all times. The grid generator employed in this work, *delaundo* [17], creates triangular grids based on the Frontal Delaunay method. Figure 3 shows the unstructured grid employed in the liquid drop computations.

A finite volume approach with a cell-centered scheme is chosen to solve the governing equations of the two phases. The integration of the governing equations (Eq.(1)) for the triangular control volume in Fig. 2 yields:

$$\frac{\Delta\left((\mathbf{W}_g)_{cn}\Delta\nu_{cn}\right)}{\Delta t^*}+\frac{\Delta\left((\mathbf{W}_g)_{cn}\Delta\nu_{cn}\right)}{\Delta t}+\sum_i\left(\mathbf{F}_c-\mathbf{F}_v\right)_i\bullet\hat{n}_i\Delta S_i=0 \tag{11}$$

where $\Delta\nu_{cn}$ denotes the volume of the triangular cell *cn*. $(\mathbf{W}_g)_{\mathrm{cn}}$ represents $\mathbf{W}_g$ estimated using the cell-centered values of *cn*. The summation is carried out over the three boundaries - *i1*, *i2* and *i3* - of *cn*. ΔS_i denotes the surface area of boundary *i* of *cn*. $\hat{n}_i$ is the unit normal vector to boundary *i*, which is directed outward from the control volume *cn*. $(\boldsymbol{F}_c)_i$ and $(\boldsymbol{F}_v)_i$ denote the convective and viscous fluxes transported across the boundary *i* into the control volume *cn*. $(\boldsymbol{F}_v)_i$ is evaluated by applying the Gauss divergence theorem, while $(\boldsymbol{F}_c)_i$ is estimated by employing the *local characteristic* approach in a total-variation-diminishing (TVD) scheme [18]. The Harten-Yee upwind TVD scheme [19] has been employed in this work. The numerical scheme is second-order accurate, and reduces to first-order near regions of large gradients.

The fluxes across the interface are estimated such that the interface conditions (Eqs.(7)-(10)) are satisfied. The viscous fluxes are assumed to be continuous at the interface. Since the interface moves with fluid velocity (Eq.(7)), i.e., $\vec{V}_s=\vec{V}_g=\vec{V}_l=\vec{V}_{int}$, the convective flux is due to pressure alone (Eq.(2)). Assuming boundary surface *i1* in Fig. 2 represents an interface boundary element, the convective flux is estimated as follows:

$$\left(\mathbf{F}_c\bullet\hat{n}\right)_{i1}=\frac{1}{2}\left(\left(\mathbf{F}_c\right)_{cn}+\left(\mathbf{F}_c\right)_{j1}\right)\bullet\hat{n}_{i1}\pm\frac{1}{2}\sigma\kappa\begin{pmatrix}0\\ \vec{\vec{\mathrm{I}}}\\ \vec{V}_{int}\end{pmatrix}_{i1}\bullet\hat{n}_{i1} \tag{12}$$

In Eq.(12), the pressure employed for evaluating $(\boldsymbol{F}_c)$ is the average of the pressures in the gas and liquid phases on either side of the interface boundary element, i.e., average of pressures in triangles *cn* and *j1*. The flux due to surface tension in Eq.(12) has a positive value for the control volume in the liquid phase and a negative value for the gas phase. This numerical treatment of the flux at the interface ensures that the jump in normal momentum flux is σκ and for the energy equation it is $\sigma\kappa(\vec{V}_{int}\bullet\hat{n})_{i1}$.

For the flow boundaries, illustrated in Fig. 3, the solution of the local one-dimensional inviscid (LODI) system of equations [20] is employed to specify the boundary conditions. The slip condition is enforced and gradients of variables are set to be zero for the

axisymmetry boundary. In the solid sphere computations, no-slip condition is enforced for velocity, pressure is obtained by assuming zero normal gradients and an adiabatic condition is imposed for temperature.

2.4. Grid movement strategies

The vertices on the boundary of the computational domain are moved with a constant velocity in the axial direction at each time step. For example, the vertices on the flow boundary are moved with the center of mass velocity of the moving body, e.g., drop or solid sphere. The movement of the vertices on the interface is governed by Eq.(7). The vertices in the interior of the domain are moved by defining velocities based on the spring tension analogy [21], which preserves the connectivity of the grid. A prescribed check on the angles of each triangle is carried out at every physical time step, along with a check for grid line crossing. If the prescribed check is violated, the grid is re-generated. The computed solution is then interpolated from the old grid to the new grid, such that the mass, momentum and energy are conserved.

For moving grids, the cell volumes are computed by solving the Geometric Conservation Law (GCL) [22]:

$$\frac{\partial \mathcal{V}}{\partial t} = \iint_{S(t)} \vec{V}_s \bullet \hat{n} \, \mathrm{d}S \tag{13}$$

The GCL is solved numerically using the same scheme that is employed for integrating the governing equations of the two fluids.

2.5. Time discretization

A second-order time accurate implicit scheme is adopted for solving the governing equations of the two phases along with the GCL. Equation (11) is discretized at physical time level $n+1$ as follows:

$$\frac{\Delta\left((\mathbf{W}_g)_{cn}\Delta\mathcal{V}_{cn}\right)}{\Delta t^*} + \left(\frac{3(\mathbf{W}_g)_{cn}^{n+1}\Delta\mathcal{V}_{cn}^{n+1}}{2\Delta t^{n+1}} - \frac{4(\mathbf{W}_g)_{cn}^{n}\Delta\mathcal{V}_{cn}^{n}}{2\Delta t^{n+1}} + \frac{(\mathbf{W}_g)_{cn}^{n-1}\Delta\mathcal{V}_{cn}^{n-1}}{2\Delta t^{n+1}} \right) + \left[\sum_i \left(\mathbf{F}_c - \mathbf{F}_v\right)_i \bullet \hat{n}_i \Delta S_i \right]^{n+1} = 0 \tag{14}$$

where the superscripts on each term denotes the physical time level at which the term is evaluated. Δt^{n+1} denotes the change in physical time from time level n to $n+1$. The solution at physical time level $n+1$ is obtained by marching Eq.(14) to a steady state in pseudo-time. The pseudo-time marching is carried out using a four-stage Runge-Kutta scheme as follows:

$$\left[1 + \Omega_m \frac{3(\Delta t^*)_{cn}}{2(\Delta t)_{cn}}\right] \left((\mathbf{W}_g)_{cn}\Delta\mathcal{V}_{cn}\right)^m = \left((\mathbf{W}_g)_{cn}\Delta\mathcal{V}_{cn}\right)^0 - \Omega_m (\Delta t^*)_{cn} \mathbf{G}_{cn}^{m-1} \tag{15}$$

where $\Omega_m = 1/(5-m)$ represents the coefficients and m denotes the stage number of the Runge-Kutta scheme, i.e., m=1,2,3,4. m=0 superscript represents variable values before the first stage integration of the Runge-Kutta scheme. $(\Delta t^*)_{cn}$ is the local change in pseudo-time for the control volume cn, and is defined to be a constant fraction of $(\Delta t)_{cn}$, where the constant depends on the problem being solved**.** The local physical time step for each triangle cn, $(\Delta t)_{cn}$, is estimated by a procedure described by Mavprilis et al. [23]. The term $3(\mathbf{W}_g)_{cn}^{n+1}\Delta\mathcal{V}_{cn}^{n+1}/2\Delta t^{n+1}$ in Eq.(14) is treated implicitly at each stage of the Runge-Kutta scheme, i.e., it is considered to be evaluated at stage m in Eq.(15). $\mathbf{G}_{cn}$ represents all the terms in Eq.(14) other than $3(\mathbf{W}_g)_{cn}^{n+1}\Delta\mathcal{V}_{cn}^{n+1}/2\Delta t^{n+1}$ and the pseudo-time term.

The unsteady flow calculation is carried out as a series of steady state calculations in pseudo-time. Since physical time is fixed when marching in pseudo-time, it is possible to employ

standard convergence acceleration techniques like local time-stepping for pseudo time and evaluation of viscous fluxes only during the first two stages of the Runge-Kutta scheme.

3. Results and discussion

The accuracy of the compressible code is assessed by computing the steady drag coefficient for a stationary solid sphere at Mach number of 0.03, which is close to the incompressible limit. Figure 4 shows the computed drag coefficient, C_d, as a function of the Reynolds number, *Re*. In the same figure, the experimental C_d measured by Roos and Willmarth [24] for glycerine-water mixtures is also plotted. The computed results show good agreement with the experimental values. Differences at higher Reynolds numbers are likely to be the result of domain size and numerical resolution effects [25].

Kim et al. [9] solved the Navier-Stokes equations for a solid sphere injected into a stagnant incompressible fluid. They presented transient variation of C_d for the decelerating solid sphere as a function of non-dimensional time, defined as $(t\ V^0)/R$, where V^0 is the initial velocity of the sphere and R is the sphere radius. The computed transient C_d for $\rho_{solid} / \rho_g = 5$ and initial $Re = 150$ is shown in Fig.5 along with the results of Kim et al.[9]. The computed results compare reasonably well with the data of Kim et al. Differences between the two solutions may arise from the fact that Kim et al. solve incompressible equations, whereas we solve the compressible equations in the fluid surrounding the solid sphere.

A classical problem that is often employed to assess the accuracy of numerical codes for drop studies is the *oscillating drop problem*. An analytical solution for the small oscillations of a liquid drop about its spherical shape has been presented by Lamb [26]. The analytical frequency of oscillation, ω, is given as $\omega^2 = 24\ \sigma / R^3\ [3\rho_l+2\rho_g]$. In the computation, $R = 1$ *cm*, $\rho_g = 1\ kg/m^3$, $\sigma = 4700\ N/m$, $\mu_g = 1.787\text{x}10^{-5}\ N\text{-}s/m^2$, $\rho_l / \rho_g = 100$ and $\mu_l / \mu_g = 35000$. Initially both the air and liquid drop are at rest. Figure 6a shows the computed interface of the liquid drop at different times. It can be observed that the initially perturbed interface oscillates about a mean circular shape. Figure 6b shows the decaying amplitude of oscillations of the liquid drop. The computed time period of oscillation is 0.326 *ms*, which is 1.56% higher than the analytical value of 0.321 *ms*. For $\rho_l / \rho_g = 1000$, the computed time period is 1.024 *ms*, which is 1.14% higher than the analytical value of 1.0125 *ms*.

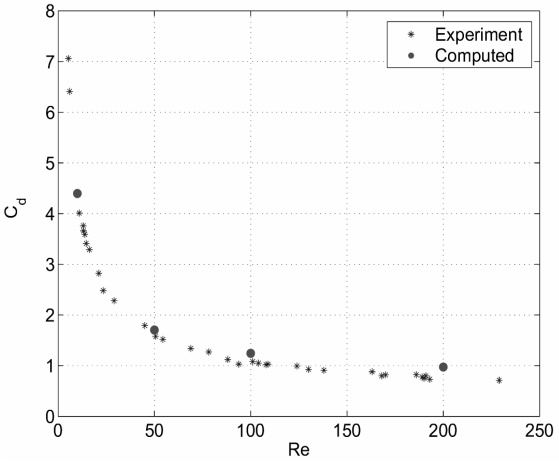

Fig. 4 Comparison of computed C*d* as a function of *Re* with experimental data of Roos and Willmarth [24].

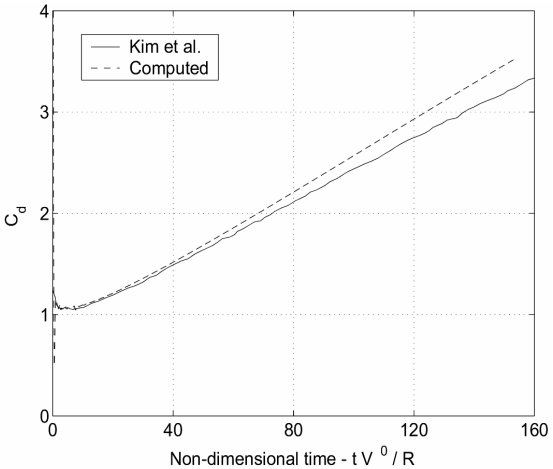

Fig. 5 Comparison of transient drag coefficient for a decelerating solid sphere with the computed data of Kim et al. [9].

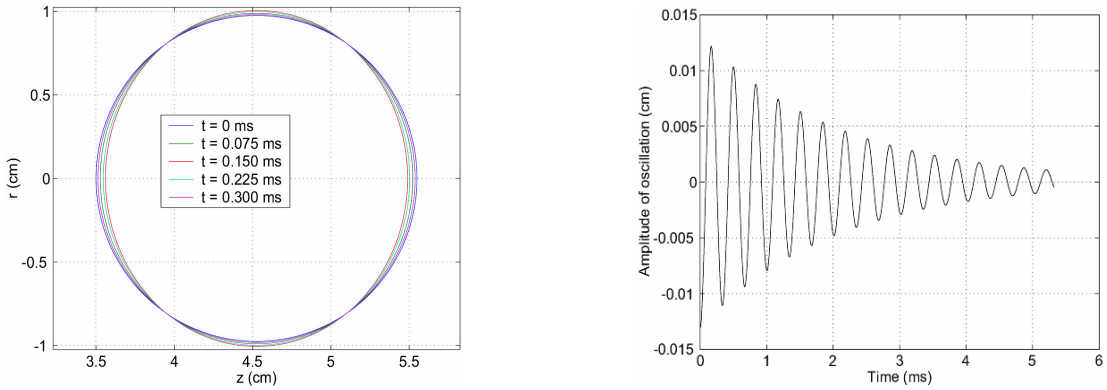

Fig. 6 Computed (a) interface and (b) amplitude of oscillation as a function of time for an oscillating liquid drop ($\rho_l / \rho_g = 100$).

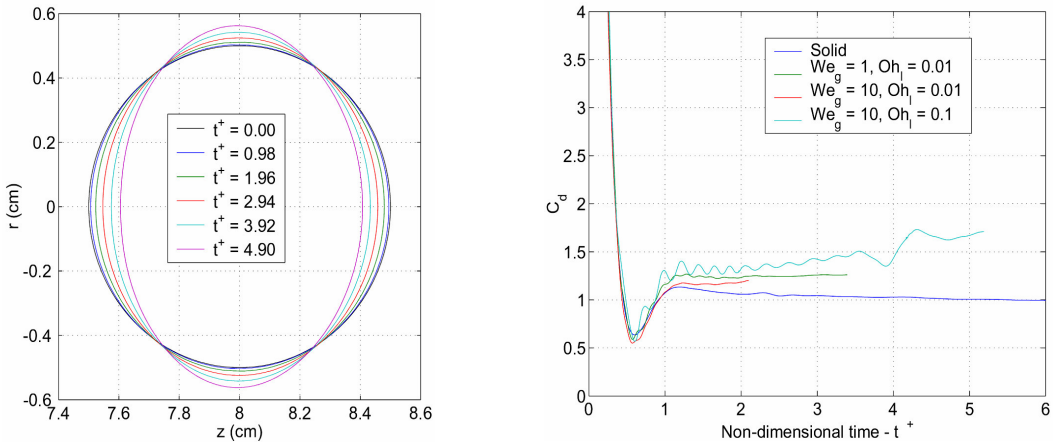

Fig. 7 Computed (a) interface for (We=10, Oh_l=0.1) and (b) transient C_d for decelerating solid sphere and liquid drops.

Computations were carried out for a decelerating solid sphere and liquid drops, which were placed initially with a velocity of $V^0 = 70$ *m/s* in stagnant air at $\rho_g = 1.2$ *kg/m*^{3} and $p_g = 1$ *atm*. The density ratio of the solid/drop to the ambient air is 50 and the initial radius is $R = 0.5$ *cm*. Based on the relative velocity of the solid/drop and air, initial $Re_g = 150$. Computations for the drops were carried out for the following initial conditions: ($We_g = 1$, $Oh_l = 0.01$), ($We_g = 10$, $Oh_l = 0.01$) and ($We_g = 10$, $Oh_l = 0.1$). The computed interface for ($We = 10$, $Oh_l = 0.1$) at different non-dimensional times, $t^+ = tV^0/R$, is shown in Fig.7a. At $t^+ = 2.94$, the drop is observed to deform noticeably from its initial spherical shape. Figure 7b shows the computed transient drag coefficient for the decelerating drops and solid sphere. C_d for the drops is observed to be higher than that for the sphere because of deformation, as shown in Fig.7a. Increasing Oh_l at $We_g = 10$, leads to higher drag, which could be attributed to higher viscous shear stress at the interface, resulting from higher viscosity of the liquid drop. At $Oh_l = 0.01$, increasing We_g, leads to decreased surface tension and hence, increased deformation and higher drag. Computed C_d values are higher for the $We_g = 1$ at $t^+ = 2$ but the rate of increase of C_d appears to higher for $We_g = 10$.

4. Summary and conclusions

A hybrid compressible-incompressible numerical method, which employs a pre-conditioned form of the compressible flow equations, is developed for computing transient flows past

drops at all Mach numbers and employed to investigate the interaction of moving drops with ambient gas. An artificial compressibility method is employed to solve the incompressible flow in the liquid phase. A finite volume numerical discretization is employed in this interface tracking method. Comparisons of computed steady state drag of a solid sphere with experimental results at several Reynolds numbers, transient drag of a solid sphere with prior numerical computations reported in the literature, and oscillating drop frequency with analytical results show adequate agreement. Initial results of transient drag coefficients for decelerating drops indicate that they are larger than for a corresponding solid sphere on account of drop deformation.

5. References

[1] Qian J and Law C K 1997 *J. Fluid Mech* **331** 59-80
[2] Post S L and Abraham J 2002 *Int. J. Multiphase Flow* **28** 997-1019
[3] Nobari M R H, Jan Y-J and Tryggvason G 1996 *Phys. Fluids* **8** 29-42
[4] Nobari M R H and Tryggvason G 1996 *AIAA J.* **34** 750-5
[5] Lafaurie B, Nardone C, Scardovelli R, Zaleski S and Zanetti G 1994 *J. Comp. Phys.* **113** 134-147
[6] Rieber M and Frohn A 1995 *J. Aerosol Sci.* **26** S929-S930
[7] Magi V 1987 *Department of Mechanical and Aerospace Engineering, Princeton University, Report No.* 1793
[8] Amsden A A, O'Rourke P J and Butler T D 1989 *LANL Technical Report* LA-11560
[9] Kim I, Elghobashi S and Sirignano W A 1998 *J. Fluid Mech.* **367** 221-253
[10] Clift R, Grace J R and Weber M E 1978 *Bubbles, Drops and Particles* (San Diego: Academic Press)
[11] Sirignano W A 1999 *Fluid Dynamics and Transport of Droplets and Sprays* (Cambridge: Cambridge University Press)
[12] Crowe C, Sommerfeld M and Tsuji Y 1998 *Multi-phase Flows with Droplets and Particles* (CRC Press)
[13] Helenbrook B T and Edwards C F 2002 *Int. J. Multiphase Flow* **28** 1631-57
[14] Temkin S and Mehta H K 1982 *J. Fluid Mech.* **116** 297-313
[15] Pletcher R H and Chen K-H 1993 *AIAA-93-3368-CP*
[16] Gaitonde A L 1998 *Int J. Numer. Meth. Fluids* **41** 1153-66
[17] http://www.cerfacs.fr/~muller/grids.html
[18] Wadhwa A R, Magi V and Abraham J 2003 *ILASS Americas, 16th Annual Conference on Liquid Atomization and Spray Systems, CA*
[19] Yee H C 1989 *NASA Technical Memorandum* 101088
[20] Poinsot T J and Lele S K 1992 *J. Comp. Phys.* **101** 104-129
[21] Venkatakrishnan V and Mavriplis D J 1995 *AIAA Paper 95-1705-CP*
[22] Thomas P D and Lombard C K 1979 *AIAA J.* **17** 1030-37
[23] Mavriplis D J, Jameson A and Martinelli L 1989 *AIAA Paper 89-0120*
[24] Roos F W and Willmarth W W 1971 *AIAA J.* **9** 185-291
[25] Wadhwa A R 2003 *Numerical Investigations of Drag Coefficients of Drops in Accelerating and Decelerating Flows, PhD thesis, Department of Mechanical Engineering, Purdue University*
[26] Lamb H 1945 *Hydrodynamics* (New York: Dover Publications)